ADVANCED ENERGY MATERIALS
www.advenergymat.de

Composite Lithium Metal Structure to Mitigate Pulverization and Enable Long-Life Batteries

*Sicen Yu, Shen Wang, Qiushi Miao, Zeyu Hui, Gayea Hyun, John Holoubek, Xiaolu Yu, Junwei Gao, and Ping Liu**

In lithium metal batteries, non-uniform stripping of lithium results in pit formation, which promotes subsequent non-uniform, dendritic deposition. This viscous cycle leads to pulverization of lithium which promotes cell shorting or capacity degradation, symptoms further exaggerated by high electrode areal loading and lean electrolytes. To address this challenge, a composite lithium metal anode is engineered that contains uniformly distributed, nanometer-sized carbon particles. This composite lithium is shown to strip more uniformly since the growth of non-uniform pits is intercepted by the carbon particles. This mechanism is corroborated by a continuum electrochemical model. Subsequent lithium deposition on carbon particles is also found to be more uniform than on the surface with irregular pits. Notably, the pulverization rate of composite lithium is 26 times slower than that of commercial lithium. Moreover, in a Li-S battery with sulfurized polyacrylonitrile cathode, the use of the composite anode extends the cycle life by three times when the areal capacity is 8 mAh cm^{-2}. The approach of using an engineered lithium composite structure to address challenges during both stripping and plating can inform future designs of lithium metal anodes for high areal capacity operations.

1. Introduction

Lithium metal batteries (LMBs) promise high energy densities for next generation electronics and electric vehicles.[1] Yet, poor reversibility of lithium (Li) plating and stripping has limited their cycle life. Li metal is gradually pulverized, which yields a porous structure with a high surface area.[2] Inside, Li metal can be either connected or isolated, and is covered by solid electrolyte interface (SEI) layers resulting from the reaction between Li and the electrolyte.[3] Advances in electrolyte design, especially localized high concentration electrolytes and ionic-liquid electrolytes, as well as the use of protective coatings and three-dimensional (3D) hosts, have greatly improved the cycle life of LMBs.[4]

The majority of the research has focused on the lithium plating process. In contrast, the lithium stripping step is much less investigated. Yet, the role of stripping is critical. For systems that use a non-lithium containing cathode, such as sulfur, the first discharge involves lithium stripping.[5] Even for those that start with deposition when a lithiated cathode is used, e.g., a lithium metal oxide, subsequent stripping is also important. One peculiar phenomenon in lithium metal batteries is that a battery made with a large access of lithium metal can fail suddenly, sometimes even faster than one made with a thinner lithium.[6] Later, it is revealed that this is due to pit formation. During stripping, pits are formed and propagate as dictated by metallurgical nonuniformities (such as grain boundaries, slip lines, and impurities).[7] During subsequent plating, lithium tends to nucleate and grow inside of pit mouth, usually leading to a porous structure.[8] Pit formation is due to local accelerated stripping, initiated by the uneven breakdown of the protective passivation layer.[9] According to Gireaud et al., pitting occurs primarily on slip lines, and the shape of the resulting pits is influenced by the viscosity of the electrolyte mixture. For instance, they have observed elongated hole shapes (up to 350 μm in size) in EC (ethylene carbonate)-$LiPF_6$, whereas circular pits with diameters of 60–70 μm are formed in EC/DMC (dimethyl carbonate)-$LiPF_6$.[9c] Later, Sanchez et al. have observed that pit morphology is impacted by surface microstructural features, where preferential pit propagation is along a grain boundary but not exclusively.[7b] Hyun et al. reported that once pits are formed at the beginning, stripping occurs almost solely from these pits.[10] Through operando optical microscopy, they demonstrated that Li tends to preferentially deposit on the pit surfaces

S. Yu, Q. Miao, X. Yu, J. Gao, P. Liu
Program of Materials Science and Engineering
University of California
La Jolla, San Diego, CA 92093, USA
E-mail: piliu@eng.ucsd.edu
S. Yu, S. Wang, Q. Miao, Z. Hui, G. Hyun, J. Holoubek, X. Yu, J. Gao, P. Liu
Sustainable Power and Energy Center
University of California
La Jolla, San Diego, CA 92093, USA
S. Wang, Z. Hui, G. Hyun, J. Holoubek, P. Liu
Department of NanoEngineering and Chemical Engineering
University of California
La Jolla, San Diego, CA 92093, USA
P. Liu
Program of Chemical Engineering
University of California
La Jolla, San Diego, CA 92093, USA

The ORCID identification number(s) for the author(s) of this article can be found under https://doi.org/10.1002/aenm.202302400

DOI: 10.1002/aenm.202302400

rather than on un-stripped areas. In addition, several studies reported that pitting behavior can trigger the formation of isolated lithium, where active Li metal under initial passive region can be gradually isolated by SEI during striping/plating cycles.[11]

It is thus essential to develop strategies to break this vicious cycle of porous lithium buildup due to the interplay between pitting and subsequent deposition. Since electrochemical stripping is preferred in regions with lower charge transfer resistance, the chemical uniformity of lithium surface plays an important role. Introducing a potentiostatic pulse to oxidize/activate the lithium surface could result in more homogeneous subsequent lithium stripping. Larger pulse currents produce more, smaller pits.[12] A mechanical rolling method was used to fabricate a highly rough but uniform lithium surface, which also render uniform lithium stripping.[13] Additionally, several studies found that Li foil with a uniform pre-passivation layer can undergo uniform stripping without pitting.[11b,14] Shi et al. reported that the start of pitting is caused by the accumulation of voids and is linked to the kinetics of void formation. Therefore, they suggested that increasing the current density during stripping can reduce the size of the pits.[15] Despite these progress, there have been very few materials solutions to mitigating the pit formation issue. Further, any such solutions need to be effective in conditions similar to those encountered in practical batteries, i.e., high areal capacity and lean electrolyte amount.

Here, we report a carbon particle infused lithium metal composite (C-Li) that has the intrinsic ability of intercepting pit propagation during lithium stripping. This design dramatically slows down the pulverization of lithium. As a result, significant performance improvement is observed in Li|Li symmetric cells, as well as in full cells where Li is paired with a sulfurized polyacrylonitrile (SPAN) cathode, at a lean electrolyte condition (2.2 g Ah^{-1}). This study demonstrates that the cycle life of LMBs depends not only on lithium plating, but also on proper lithium stripping. Overcoming the non-uniformity induced by stripping can provide new directions for enhancing the cycle life of lithium metal batteries.

2. Results and Discussion

2.1. Design and Fabrication of Carbon Doped Li (C-Li)

Figure 1 illustrates the conceptual design of the composite Li metal, as well as its impact on the morphological evolution of Li during stripping-plating cycles. We highlight two distinct modes: the commercial Li foil, herein referred to as P-Li, characterized by the formation of pits (Figure 1A), resulting in highly porous and dendritic Li deposition after a single cycle; and carbon doped Li, or C-Li, in which carbon particles have some ability to mitigate pit propagation (Figure 1B), leading to subsequent uniform and low-porosity Li deposition. The variations in Li porosity and its build-up rate significantly impact the cycle life of LMBs. Under high electrolyte/capacity (E/C) ratios (Figure 1C), batteries utilizing C-Li exhibit an extended cycle life due to reduced challenges from dendritic Li compared to those using P-Li, which tends to fail due to shorting. Under low E/C ratios (Figure 1D), batteries utilizing C-Li demonstrate a longer cycle life than those using P-Li, as they are less likely to suffer from electrolyte dry out due to a lower rate of pulverization and increase in porosity.

We utilize an accumulative roll bonding (ARB) technique to fabricate C-Li. Ketjen black (KB) is used as a typical carbon material (particle size: 30 nm) at a 5 wt.% loading based on the mass of Li foil. The process involves adding carbon particles onto a commercial lithium foil, followed by repetitive rolling and folding at room temperature (**Figure 2**A; Figure S1, Supporting Information). Commercial Li foil, P-Li, has a thickness of 100 μm (Figure 2B). C-Li produced through ARB also maintains a thickness of 100 μm (Figure 2E). P-Li exhibits noticeable boundaries and impurities (Figure 2C,D). In contrast, C-Li exhibits a uniform texture, where carbon particles are uniformly distributed within the C-Li structure (Figure 2F,G; Figure S1C,E, Supporting Information).

2.2. Pitting during Lithium Stripping

To understand the anti-pitting mechanism of C-Li, stripping experiments are conducted at a current density of 0.5 mA cm^{-2} with LDME as the electrolyte (2 M lithium bis(fluorosulfonyl)imide (LiFSI) in 1,2-dimethoxyethane/bis(2,2,2-trifluoroethyl) ether (DME/BTFE) with a weight ratio of 1:4). The SEM images of C-Li and P-Li after stripping different capacities of Li are shown in **Figure 3**A,B and Figure S2 (Supporting Information). The size of pits is defined as the area of a connected stripped lithium region (one pit and/or interconnected pits). We performed image analysis using Image J software and calculated the stripped area ratio, which is defined as the ratio of the stripped area over the total area of the SEM image. The results of this analysis are presented in Figure 3C. At the initial stage of lithium stripping (0.5 mAh cm^{-2}), P-Li and C-Li display distinct behaviors. In P-Li, pits are of various shapes and sizes (>500 μm^2), and randomly distributed (Figure 3A; Figure S2A, Supporting Information). In contrast, pits in C-Li are smaller (<200 μm^2) and evenly distributed (Figure 3B). At a stripping capacity of 1 mAh cm^{-2}, the pit size of C-Li surpasses that of P-Li, as a result of more pits forming on the surface of C-Li and subsequently merging together (Figure S2F, Supporting Information). In contrast, pits on P-Li remain isolated and randomly distributed (Figure S2B, Supporting Information). With a stripping capacity larger than 3 mAh cm^{-2}, nearly 100% of the C-Li surface is stripped (Figure 3C). In contrast, pit propagation is observed in P-Li (Figure S2C,D, Supporting Information), and the stripped area ratio remains low (<40%) even when the stripping capacity reaches 6 mAh cm^{-2}. These results suggest that incorporating carbon can change the pit propagation mode from predominantly vertical to lateral, finally leading to a uniform lithium stripping process, aligning well with what was proposed in the schematic diagram shown in Figure 1A,B. This effect is verified across four different electrolytes (Figures S3,S4, Supporting Information).

We also examined the effect of current density on pit formation (Figure S5, Supporting Information). C-Li exhibits uniform stripping at all three current densities. In contrast, as the current density increases from 0.5 to 3 mA cm^{-2}, pitting behavior on P-Li becomes less severe with smaller pit sizes and more uniformly distributed pits. Hence, the enhancement in performance by the introduction of carbon is most pronounced at modest current densities, which are most commonly used in the testing of lithium metal batteries.[6] The stripping mode characterized by a

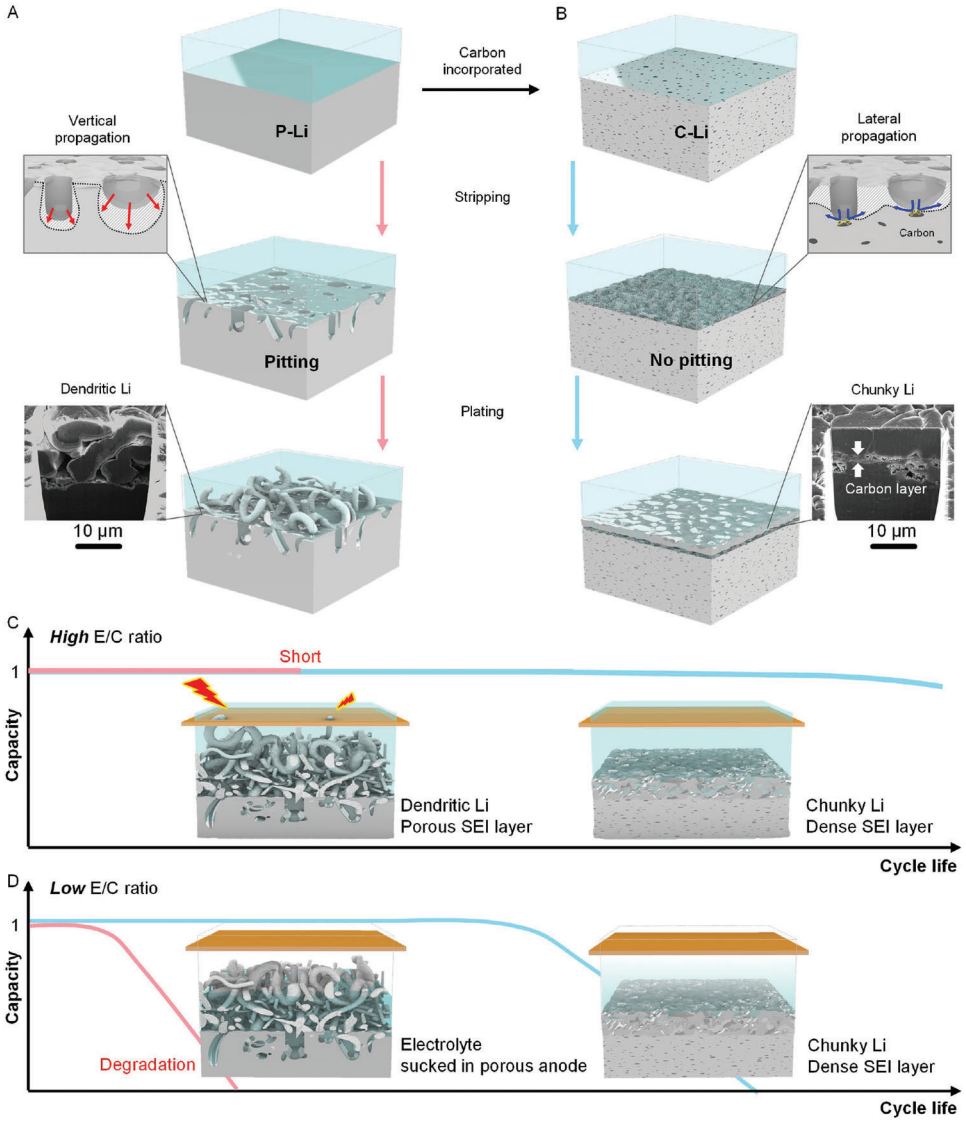

Figure 1. Carbon doping to break the vicious cycle of Li pulverization. Schematic diagrams of lithium striping-plating behavior of A) commercial lithium foil (P-Li) and B) carbon incorporated lithium foil (C-Li). Inset scanning electron microscopy (SEM) images show cross-sectional views of 3 mAh cm^{-2} of Li deposited on P-Li and C-Li after stripping 6 mAh cm^{-2} of Li, at the same current density of 0.5 mA cm^{-2}, respectively. Schematic diagrams of capacity retention versus cycle life of full cells using P-Li (Red lines) and C-Li as anodes (Blue lines), under C) high electrolyte/capacity (E/C) ratios and D) low E/C ratios, respectively.

consistent percentage of the stripped area regardless of the stripping capacity, such as in P-Li (blue in Figure 3C), is referred to as pitting stripping. In contrast, the stripping mode exemplified by C-Li (red in Figure 3C), where the extent of the stripped area is directly linked to the stripping capacity and rapidly reaches 100%, is defined as pitting-free stripping.

The distribution of carbon particles in C-Li is a critical factor in achieving pitting-free stripping. This dependence is primarily influenced by the size of carbon particles and the loading of carbon in the C-Li composite. To investigate this further, two additional experiments are conducted. First, the impact of particle size is evaluated by using different carbon particles: graphite (G) with a particle size of 2600 nm and graphene (Gr) with a particle size of 420 nm. These are employed to fabricate C-Li, referred to as G-Li and Gr-Li, respectively. The weight ratio of carbon to Li is fixed at 5:100. After being stripped of 6 mAh cm^{-2} of Li at a current density of 0.5 mA cm^{-2}, G-Li exhibits noticeable pits, whereas Gr-Li displays a uniform stripping pattern (Figure S6, Supporting Information). This can be explained by the fact that the gap between two carbon particles increases as the particle size increases, resulting in a reduced pit interception effect. Next, the effect of carbon loading on Li stripping is evaluated. Three KB-incorporated Li composites are fabricated: C1-Li (KB:Li weight ratio of 1:100), C5-Li (KB:Li weight ratio of 5:100), and C10-Li (KB:Li weight ratio of 10:100). Notably, C5-Li demonstrates the ability to strip nearly 100% of the Li surface when stripping 3 mAh cm^{-2} of Li at a current density of 0.5 mA cm^{-2} (Figure 3B). At the same current density, the stripped ratio of C10-Li reaches 100% with a stripping

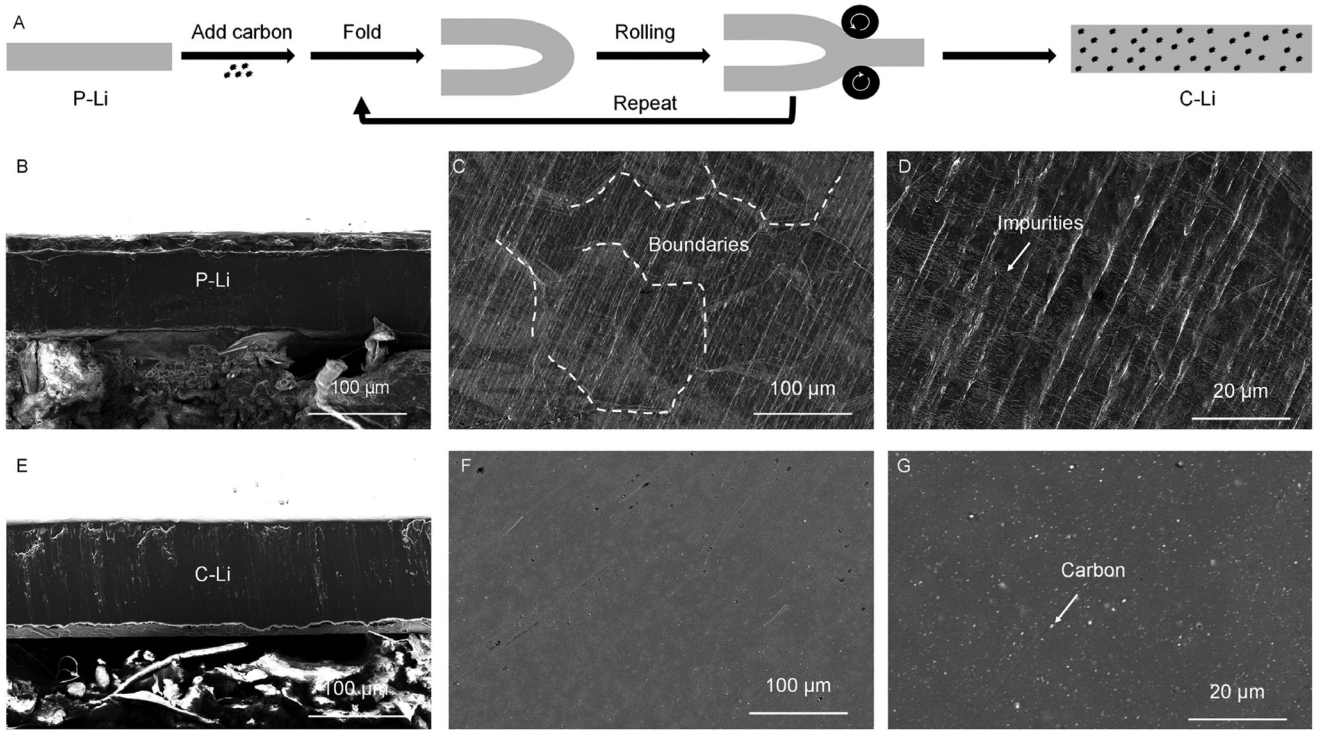

Figure 2. Fabrication and characterization of Li foils. A) Schematic diagram of C-Li fabrication via mechanical rolling. B–D) SEM images of P-Li, and E–G) SEM images of C-Li.

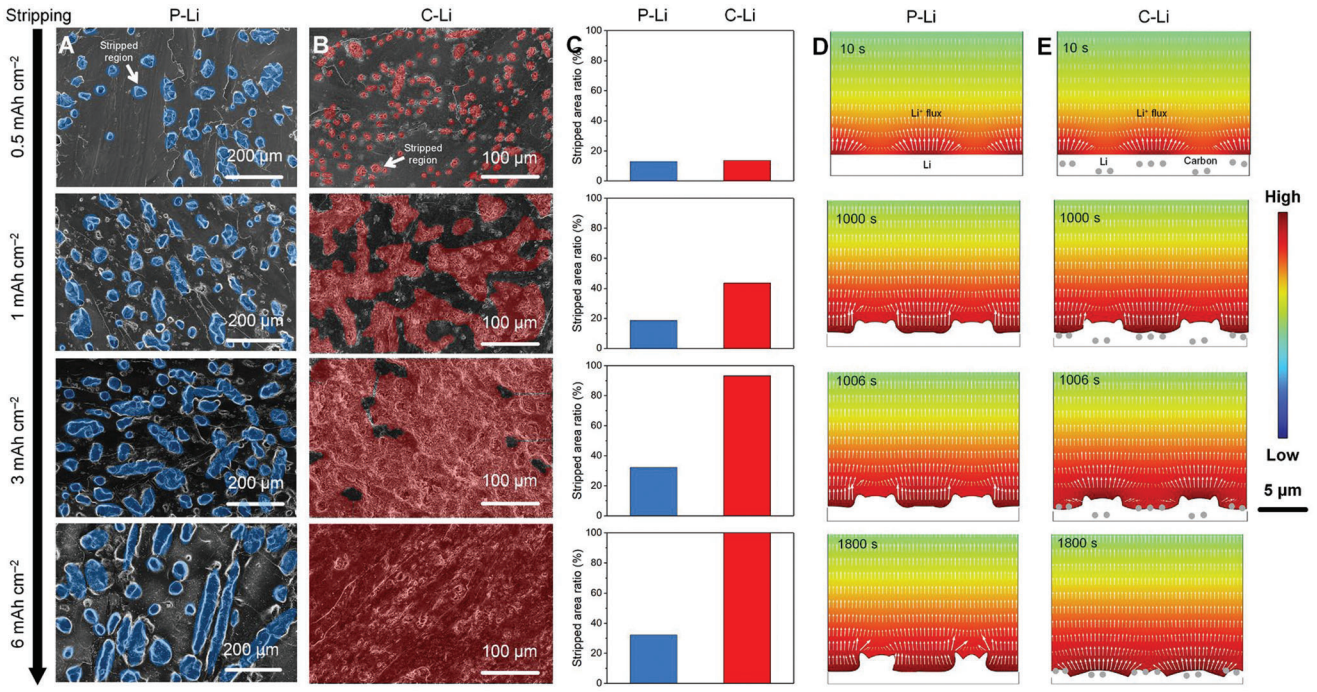

Figure 3. Carbon-doping effect on lithium stripping. Top view SEM images of A) P-Li and B) C-Li after stripping 0.5, 1, 3, 6 mAh cm^{-2} at 0.5 mA cm^{-2}, respectively. The regions labeled in blue and red represent the stripped areas and the remaining unlabeled regions are un-stripped areas. C) The stripped area analysis of (A) and (B). D) COMSOL Multiphysics simulation of the local current density distribution of P-Li during Li stripping process. E) COMSOL Multiphysics simulation of the local current density distribution of C-Li during Li stripping process. The color gradient in the visualization represents variations in the concentration of Li ions, while the arrows depict the direction and magnitude of the Li-ion flux.

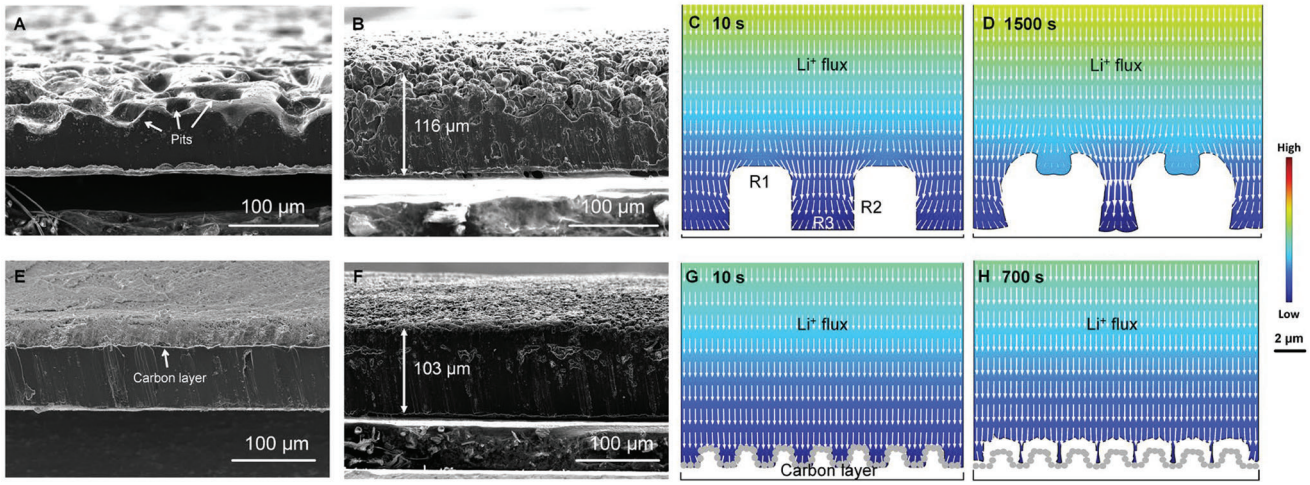

Figure 4. Stripping effect on subsequent lithium plating. A) Cross-sectional SEM image of P-Li after stripping 6 mAh cm^{-2} of Li at a current density of 0.5 mA cm^{-2}. B) Cross-sectional SEM image of the sample shown in (A) after plating 6 mAh cm^{-2} of Li at a current density of 0.5 mA cm^{-2}; C,D) COMSOL Multiphysics simulation of the local current density distribution of stripped P-Li during Li plating process. E) Cross-sectional SEM image of C-Li after stripping 6 mAh cm^{-2} of Li at a current density of 0.5 mA cm^{-2}. F) Cross-sectional SEM image of the sample in (E) after plating 6 mAh cm^{-2} of Li at a current density of 0.5 mA cm^{-2}. G,H) COMSOL Multiphysics simulation of the local current density distribution of stripped C-Li during Li plating process. The color gradient in the visualization represents variations in the concentration of Li ions, while the arrows depict the direction and magnitude of the Li-ion flux.

capacity of 2 mAh cm^{-2}, while the stripped ratio of C1-Li is only 27.3% after 6 mAh cm^{-2} of Li is stripped (Figure S7, Supporting Information). A higher loading of carbon in C-Li increases the likelihood of pits encountering a carbon particle, which essentially intercepts pit propagation. Conversely, a lower loading of carbon in C-Li reduces this effect. Hence, both carbon size and the carbon loading of C-Li composites play important roles in impeding the pit propagation process. At a given carbon mass ratio in the C-Li composite, a small carbon particle size proves advantageous in minimizing the distance between carbon particles, consequently leading to an amplified interception effect. Additionally, increasing the carbon mass ratio can also enhance the pit interception effect. Once the stripping capacity surpasses the critical capacity necessary for complete surface stripping, uniform stripping behavior persists independently of the anode thickness.

To further investigate the effect of incorporating carbon on pitting-free stripping, we employ a continuum model (COMSOL), the details of which are provided in the experimental section. We assume non-uniform reactivity for the Li stripping reaction on the electrode surface (Figure S8, Supporting Information). In the case of P-Li, throughout the entire stripping process, the reaction currents (Li^+ flux) concentrate on the more reactive surfaces, indicated by dark red regions depicting high concentration of Li ions (Figure 3D). This phenomenon leads to the formation of pits in those regions and the presence of Li islands on less reactive surfaces. On the other hand, when carbon black is incorporated into Li metal (C-Li), the initial stripping also occurs at more reactive surfaces (dark red regions) and leads to pit formation (< 1000 s, Figure 3E). However, when meeting incorporated carbon particles (1006 s, Figure 3E), pits start to stop propagation downward and instead start to move laterally with continued stripping of Li. We can see that the reaction current shifts to areas of those initially less reactive Li islands. At the same time, the concentration of Li ions on the Li islands also becomes higher than on pits, which is consistent with our proposal. With the stripping of Li islands, the carbon fillers inside also concentrate and cover the surfaces, eventually leading to a uniform carbon layer.

2.3. Stripping Effect on Subsequent Lithium Plating

Following the initial stripping, distinct features arise on the lithium surface due to variations in pitting behavior. Cross-sectional SEM images reveal that the pits formed on P-Li (**Figure 4**A) are larger and deeper compared to those on C-Li (Figure 4E). Additionally, a carbon layer consisting of exposed carbon particles is observed on the C-Li surface (Figure 4E). After subsequent plating 6 mAh cm^{-2} of Li at a current density of 0.5 mA cm^{-2}, the deposited Li on P-Li manifests as a porous structure (Figure 4B). The thickness of P-Li increases from 100 to 116 μm, equivalent to a porosity of 13.8%. On the other hand, the deposited Li on C-Li appears uniform and dense (Figure 4F), with the thickness of C-Li increasing only from 100 to 103 μm, equivalent to a porosity of 2.9%. To gain deeper understanding of the Li plating behavior following stripping, we conducted a continuum model (COMSOL). The Methods section provides detailed experimental procedures and simulation parameters. The model categorizes lithium deposition on non-uniform substrates (P-Li) into three regions: the top surface of Li islands (R1), the wall surface of pits (R2), and the bottom surface of pits (R3) (Figure 4C). Among these regions, the pit wall surface experiences the highest current density, resulting in preferential lithium deposition in that area. On the pit wall, the Li-ion concentration in the top regions is 2.51 mM higher than that in the bottom regions, further promoting preferential lithium deposition on the top region. As the Li on both sides grows upwards, a cavity forms at the bottom of the pit (Figure 4D). In contrast, the plating behavior on C-Li is distinctly different (Figure 4G,H). The

deposition process initiates on the carbon-covered Li surface. The current distribution during plating on C-Li appears to be more uniform, both on the top surface of carbon layer and on the surfaces within the pits (Figure 4G). Additionally, the substrate featuring smaller pits exhibits a greater uniformity in the distribution of Li-ion concentration among the regions R1, R2, and R3, with the variation reduced to 0.56 mM. These optimizations contribute to a more uniform deposition along all surfaces, as observed in the resulting plating morphology (Figure 4H). The uniform substrate and incorporated carbon play significant roles in influencing the plating behavior, resulting in a more controlled and uniform deposition process. We expect that the nature of carbon materials, such as surface functional groups and conductivities, may exert a more significant impact on the subsequent lithium deposition, a topic that certainly warrants further research.

2.4. The Evolution of Li Morphology during Cycling

Next, we evaluate the electrochemical performance and observe the morphological changes of P-Li and C-Li in Li|Li symmetric cells during cycling. P-Li and C-Li serve as the working electrodes, while P-Li acts as the counter electrode (**Figure 5**A). We conduct galvanostatic stripping and deposition with a current density of 1 mA cm^{-2} and a capacity of 6 mAh cm^{-2}. All cell testing begins with lithium stripping from the working electrode (Figure 5B). The voltage versus time curves illustrate that C-Li demonstrates a slower rate of overpotential increase during cycling in comparison to P-Li (Figure 5A). Specifically, within the initial 100 hours, the overpotentials of the P-Li|C-Li cell (80 mV) and the P-Li|P-Li cell (101 mV) remain stable (Figure 5B). Interestingly, the voltage curves in Figure 5B display an intriguing lack of symmetry, indicating distinct behaviors during discharge and charge processes. Specifically, the discharge voltage curves do not overlap, with the cell using P-Li as the working electrode showing a more negative shift compared to the one using C-Li. However, the charge voltage values of the two cells are similar, which is reasonable as both curves represent the process of Li stripping from counter electrodes, which are both P-Li. This suggests that the difference in overpotential is primarily attributed to variations in working electrodes (P-Li and C-Li). Upon examining their morphologies from a cross-sectional view, P-Li develops a porous top layer that is 8.4 μm thick (Figure 5E), whereas C-Li forms a thinner top layer measuring 4 μm in thickness (Figure 5H) after 120 h of cycling. We attribute the formation of this top layer to a composite of SEI, carbon particles, and isolated lithium. The accumulation of these components is believed to contribute to the observed increase in overpotential. After 300 h of cycling, the P-Li|C-Li cell maintains a stable and low overpotential of 90 mV (Figure 5C), with the thickness of the top layer on C-Li remaining at 8 μm (Figure 5I). However, the P-Li|P-Li cell experiences an increase in overpotential to 130 mV (Figure 5C), accompanied by the presence of a significant amount of porous and isolated lithium on P-Li (Figure 5F). After 1440 h of cycling, the P-Li|P-Li cells are shorted. The cell also experiences substantial polarization, particularly during the beginning and the end of each constant current step, indicating a high charge transfer resistance for deposition and difficulties in lithium transportation during stripping (Figure 5D). In contrast, the P-Li|C-Li cells continue to operate, albeit with a higher overpotential (Figure 5D). Additionally, top-view and cross-sectional SEM images reveal that P-Li has minimal active lithium left (Figure 5G; Figure S9A, Supporting Information). In contrast, C-Li still has significant active lithium (Figure S9B, Supporting Information), as evidenced by a well-preserved, shiny lithium surface when examined from the bottom (inset image in Figure 5J). These findings clearly demonstrate that the incorporation of carbon effectively retards the rate of lithium pulverization.

2.5. Full Cell Electrochemical Performance

To examine the impact of C-Li on the cycle life of lithium metal batteries, we select sulfurized polyacrylonitrile (SPAN) as the cathode material. Previous work has established that SPAN is a stable cathode material in several electrolytes and the cycle life is often limited by the lithium metal anode.[16] Here, we compare the full-cell electrochemical performance of P-Li (≈100 μm) and C-Li (≈100 μm), paired with SPAN electrodes with an areal capacity of 4–8 mAh cm^{-2}. We note that these capacity values are very high but are essential for enabling Li-SPAN batteries to offer practical energy densities. In the first set of tests, we use a mildly lean electrolyte condition (5 g Ah^{-1}) but with an areal loading of 8 mAh cm^{-2}. Based on the mass of the active stack and electrolyte (Table S2, Supporting Information), the Li-SPAN cell can achieve a projected energy density of 229 Wh kg^{-1}. The electrodes are cycled at a rate of 0.2 C (1 C of SPAN is defined as 600 mA g^{-1}, **Figure 6**A,B). The P-Li cell exhibits a lifespan of 77 cycles while the C-Li cell demonstrates an extended cycle life of 277 cycles. The failure mode is shorting rather than gradual capacity degradation. In a second set of tests, we evaluate cells at a lean electrolyte condition (2.2 g Ah^{-1}) and a rate of 0.33 C. During the first two formation cycles (0.05 C, Figure 6C), SPAN electrodes in both the P-Li cell and C-Li cell are stable, delivering an areal capacity of 4.2 mAh cm^{-2} and a specific capacity of 720 mAh g^{-1}. We note that this condition would deliver a projected energy density of 283 Wh kg^{-1}. However, under the 0.33 C cycling condition, the P-Li cell experiences rapid degradation, with its capacity decaying from >3.5 mAh cm^{-2} to nearly zero within 54 cycles. This degradation pattern is attributed to electrolyte depletion, consistent with observations in lean-electrolyte cells reported in the literature.[17] In contrast, C-Li cells maintain stability for 132 cycles before the capacity retention drops to 80% (Figure 6C). The voltage profile (Figure 6D) also indicates that C-Li experiences a slower increase in Li anode impedance. We note that C-Li is effective in both tests that feature different E/C ratios. When there is sufficient electrolyte, cells fail due to shorting, presumably a result of local dendrite growth. When the E/C is very low, electrolyte depletion becomes a limiting factor. Both failure modes, however, are related to the non-uniform stripping and deposition which lead to the formation of porous, inhomogeneous structures.

To gain insights into the significant difference in cyclability, the cells are disassembled after 20 cycles (stopped at 1 V) to examine the morphology of Li. Top view SEM images reveal isolated Li on P-Li (Figure 6E), while C-Li does not show this behavior (Figure 6G). Cross-sectional SEM images show that P-

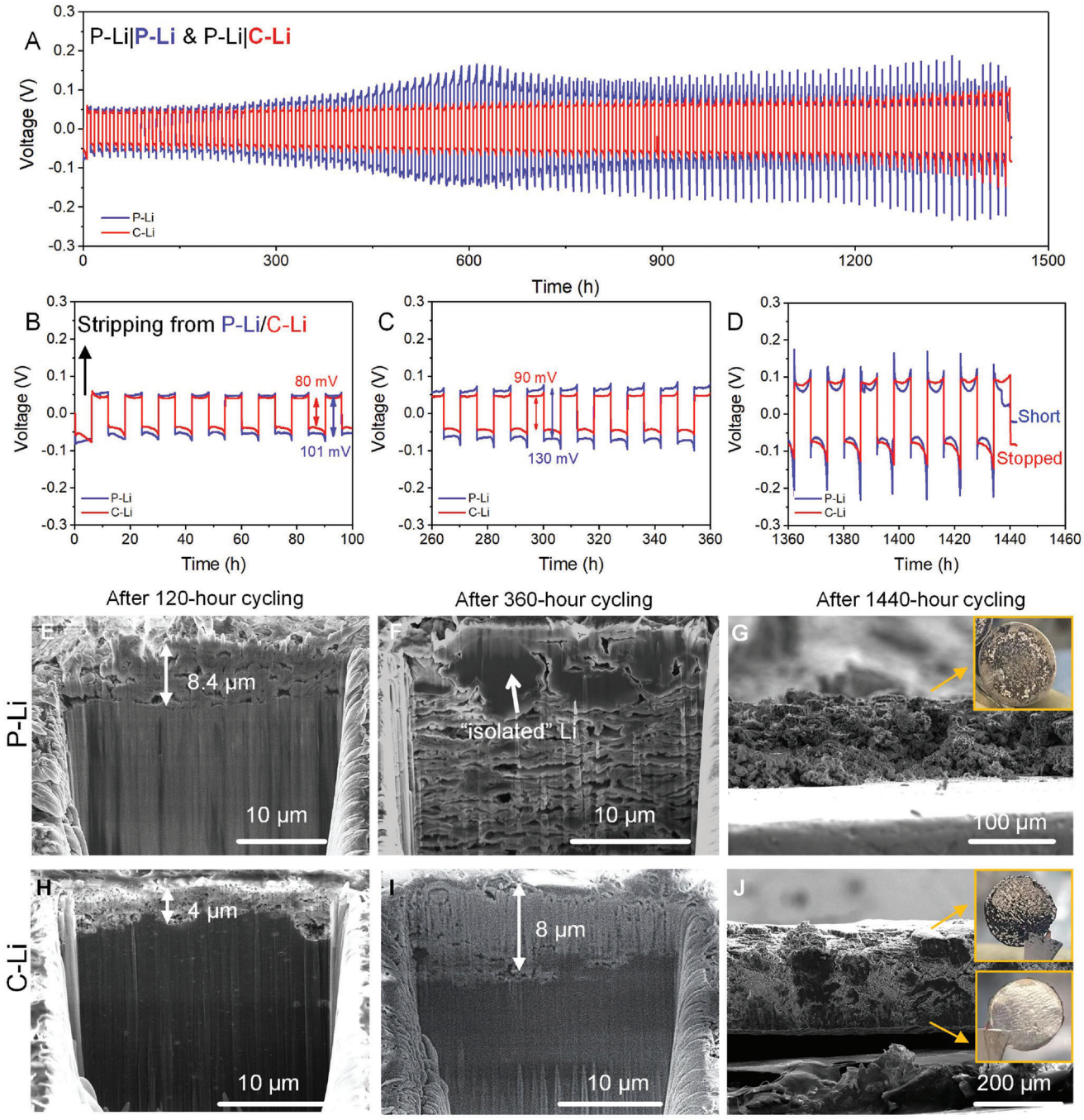

Figure 5. Lithium evaluation during stripping-plating cycles. A–D) The charge-discharge curves of P-Li|P-Li and P-Li|C-Li cells with flooded LDME electrolyte. Cross-sectional view of P-Li after the 10th E), 30th F) stripping process, and after 1440 h of cycling G), respectively. Cross-section view of C-Li after the 10th H), 30th I) stripping process, and after 1440 h of cycling J), respectively. Insets are optical images of G) and J), respectively.

Li has a porous and mossy two-layer structure consisting of a layer of lithium (99 μm) and a porous top, SEI/dead lithium layer of 50 μm (Figure 6F), consistent with observations in symmetric cells (Figure 5F). In contrast, the thickness of C-Li is 82 μm including a thin carbon-Li layer (Figure 6H). In order to obtain a deeper understanding of the top layer on C-Li, a 3D reconstruction is performed using cryo-focused ion beam (FIB)-SEM (Figure 6I). The resulting reconstruction reveals a carbon-Li layer with a thickness of 4 μm with evenly distributed pores in the structure. Notably, there are no noticeable isolated Li within the layer. Assuming the thickness of Li after the first stripping (4.2 mAh cm^{-2}) as the base value (79 μm), P-Li undergoes an expansion of 89.9%, whereas C-Li only expands by 3.8%. The pulverization rate, as defined by the ratio of expansion, of P-Li is 3.95 μm per cycle, while that of C-Li is 0.15 μm per cycle. This observation clearly demonstrates that the inclusion of carbon in

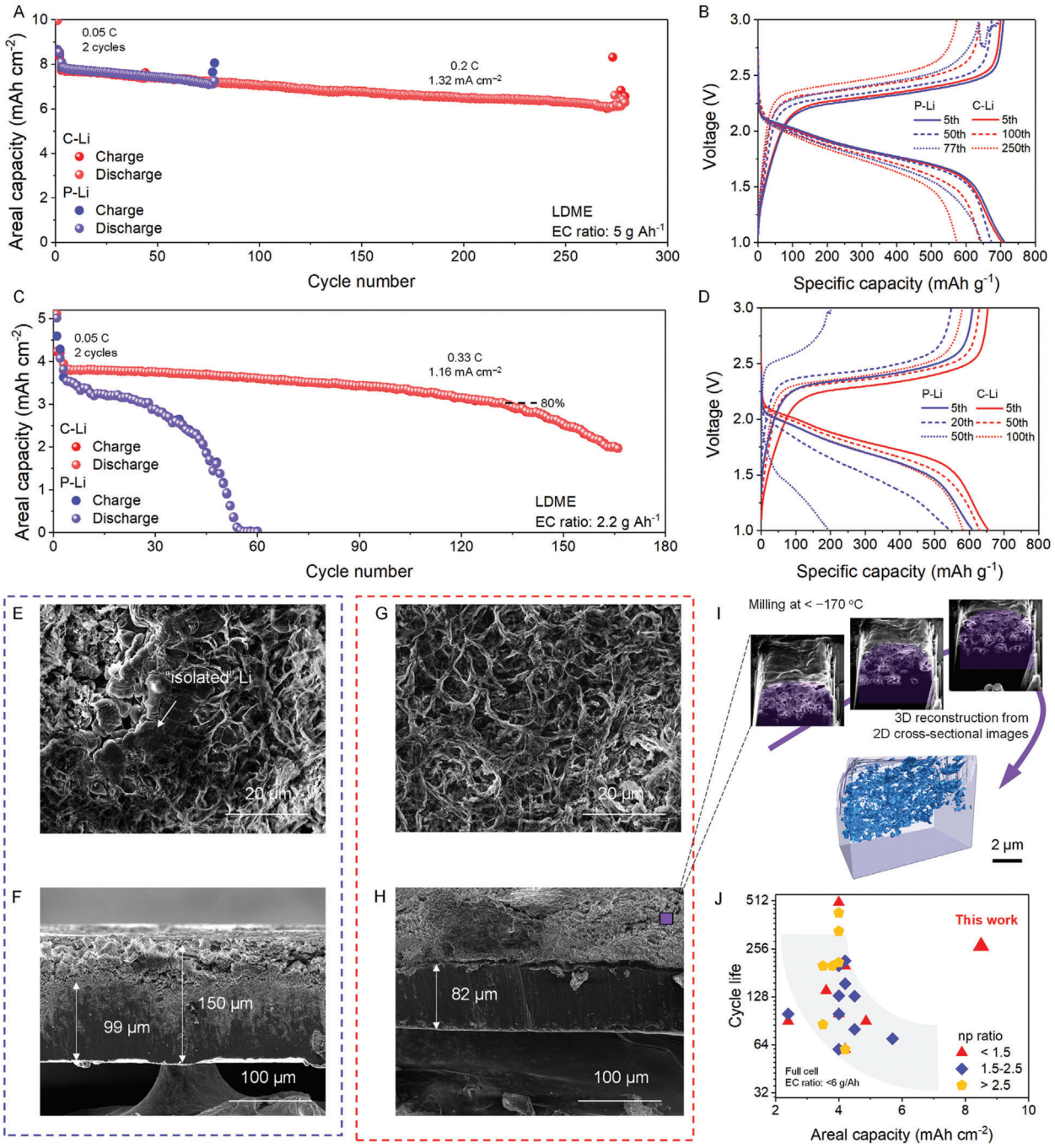

Figure 6. Full cell evaluation. A,B) Capacity retention and evolution and charge-discharge profiles of Li-SPAN cells with an E/C ratio of 5 g Ah^{-1}. C,D) Capacity retention and evolution and charge-discharge profiles of Li-SPAN cells with an E/C ratio of 2.2 g Ah^{-1}. Top view SEM images of E) P-Li, and G) C-Li after 20 cycles in (C), respectively. Cross-sectional view SEM images of F) P-Li, and H) C-Li after 20 cycles in (C), respectively. I) Three-dimension reconstruction from two-dimension cross-sectional SEM images of the cycled C-Li in (H). The purple regions are solid structures containing Li, carbon, and SEI, and the blue regions are porous structures. J) A cycle life summary of reported full cells with E/C ratios of < 6 g Ah^{-1} (Table S1, Supporting Information).

the system plays a significant role in minimizing the rate of Li pulverization.

Figure 6J presents a summary of reported data describing the relationship between the cycle life and the areal capacity of lithium metal batteries. Most reported areal capacities are approximately 4 mAh cm^{-2}, which is a reasonable value for $Li|LiNi_{0.8}Mn_{0.1}Co_{0.1}O_2$ (nickel-based cathodes) batteries but not sufficient for Li-S batteries. Even under these moderate cathode loading and E/C ratios, the cycle life is usually less than 150 cycles. However, this work demonstrates that a Li-SPAN battery

with an areal capacity of 8 mAh cm^{-2} can last 264 cycles with 80% capacity retention, which is enabled by the anti-pitting design of C-Li leading to less Li pulverization during cycling.

3. Conclusion

We have shown that incorporating carbon black particles in lithium metal can mitigate the pit propagation during lithium stripping since the carbon particles intercept the propagation of the pits and redirect the direction of stripping. This approach breaks the viscous cycle suffered by commercial lithium foils, where pit propagation is inevitable. Our observation is corroborated by a COMSOL model which describes how the stripping current is redirected at the carbon particles, leading to uniform stripping and the subsequent low-porosity Li deposition. The optimized stripping slows down Li pulverization and finally translates to longer cycle life. When evaluated in Li-SPAN full cells, the mechanism is effective in both modest (E/C ratio of 5 g Ah^{-1}) and lean electrolyte conditions (E/C ratio of 2.2 g Ah^{-1}). Overall, carbon-incorporated lithium foils show promising potential in enhancing the overall performance of lithium metal batteries. C-Li is produced by a rolling process, which is scalable and can be incorporated in standard battery manufacturing processes.

Supporting Information

Supporting Information is available from the Wiley Online Library or from the author.

Acknowledgements

This work was performed in part at the San Diego Nanotechnology Infrastructure (SDNI) of University of California San Diego, a member of the National Nanotechnology Coordinated Infrastructure (NNCI), which is supported by the National Science Foundation (Grant ECCS-1542148). This work was supported by the Office of Vehicle Technologies of the U.S. Department of Energy through the Advanced Battery Materials Research (BMR) Program (Battery500 Consortium) under Contract no. DE-EE0007764 to P.L.

Conflict of Interest

A patent disclosure is filed with University of California San Diego's Office of Innovation and Commercialization.

Data Availability Statement

The data that support the findings of this study are available from the corresponding author upon reasonable request.

Keywords

high areal capacity, lean electrolyte, lithium pulverization, long cycle life, pit formation

Received: July 25, 2023
Revised: August 29, 2023
Published online:

[1] a) J. Liu, Z. Bao, Y. Cui, E. J. Dufek, J. B. Goodenough, P. Khalifah, Q. Li, B. Y. Liaw, P. Liu, A. Manthiram, *Nat. Energy* **2019**, *4*, 180; b) D. T. Boyle, W. Huang, H. Wang, Y. Li, H. Chen, Z. Yu, W. Zhang, Z. Bao, Y. Cui, *Nat. Energy* **2021**, *6*, 487; c) D. Lin, Y. Liu, Y. Cui, *Nat. Nanotechnol.* **2017**, *12*, 194; d) X. Liang, Q. Pang, I. R. Kochetkov, M. S. Sempere, H. Huang, X. Sun, L. F. Nazar, *Nat. Energy* **2017**, *2*, 17119; e) X.-B. Cheng, R. Zhang, C.-Z. Zhao, Q. Zhang, *Chem. Rev.* **2017**, *117*, 10403.

[2] a) C. Fang, B. Lu, G. Pawar, M. Zhang, D. Cheng, S. Chen, M. Ceja, J.-M. Doux, H. Musrock, M. Cai, *Nat. Energy* **2021**, *6*, 987; b) Q. K. Zhang, X. Q. Zhang, L. P. Hou, S. Y. Sun, Y. X. Zhan, J. L. Liang, F. S. Zhang, X. N. Feng, B. Q. Li, J. Q. Huang, *Adv. Energy Mater.* **2022**, *12*, 2200139; c) X. Cao, X. Ren, L. Zou, M. H. Engelhard, W. Huang, H. Wang, B. E. Matthews, H. Lee, C. Niu, B. W. Arey, *Nat. Energy* **2019**, *4*, 796.

[3] a) C. Fang, J. Li, M. Zhang, Y. Zhang, F. Yang, J. Z. Lee, M.-H. Lee, J. Alvarado, M. A. Schroeder, Y. Yang, *Nature* **2019**, *572*, 511; b) F. Liu, R. Xu, Y. Wu, D. T. Boyle, A. Yang, J. Xu, Y. Zhu, Y. Ye, Z. Yu, Z. Zhang, *Nature* **2021**, *600*, 659.

[4] a) H. Liu, J. Holoubek, H. Zhou, A. Chen, N. Chang, Z. Wu, S. Yu, Q. Yan, X. Xing, Y. Li, *Mater. Today* **2021**, *42*, 17; b) H. Sun, G. Zhu, Y. Zhu, M. C. Lin, H. Chen, Y. Y. Li, W. H. Hung, B. Zhou, X. Wang, Y. Bai, *Adv. Mater.* **2020**, *32*, 2001741; c) X. Liu, A. Mariani, H. Adenusi, S. Passerini, *Angew. Chem., Int. Ed.* **2023**, *62*, e202219318; d) J. Xu, T. P. Pollard, C. Yang, N. K. Dandu, S. Tan, J. Zhou, J. Wang, X. He, X. Zhang, A.-M. Li, *Joule* **2023**, *7*, 83; e) J. Qian, W. A. Henderson, W. Xu, P. Bhattacharya, M. Engelhard, O. Borodin, J.-G. Zhang, *Nat. Commun.* **2015**, *6*, 6362; f) S. Chen, J. Zheng, D. Mei, K. S. Han, M. H. Engelhard, W. Zhao, W. Xu, J. Liu, J. G. Zhang, *Adv. Mater.* **2018**, *30*, 1706102; g) R. Weber, M. Genovese, A. Louli, S. Hames, C. Martin, I. G. Hill, J. Dahn, *Nat. Energy* **2019**, *4*, 683; h) S. Yu, Z. Wu, J. Holoubek, H. Liu, E. Hopkins, Y. Xiao, X. Xing, M. H. Lee, P. Liu, *Adv. Sci.* **2022**, *9*, 2104829; i) L. Liu, Y.-X. Yin, J.-Y. Li, N.-W. Li, X.-X. Zeng, H. Ye, Y.-G. Guo, L.-J. Wan, *Joule* **2017**, *1*, 563; j) H. Chen, A. Pei, J. Wan, D. Lin, R. Vilá, H. Wang, D. Mackanic, H.-G. Steinrück, W. Huang, Y. Li, *Joule* **2020**, *4*, 938; k) Y. Gao, Z. Yan, J. L. Gray, X. He, D. Wang, T. Chen, Q. Huang, Y. C. Li, H. Wang, S. H. Kim, T. E. Mallouk, D. Wang, *Nat. Mater.* **2019**, *18*, 384; l) L. Tao, B. Ma, F. Luo, Z. Xu, Z. Zheng, H. Huang, P. Bai, F. Lin, *Nano Energy* **2022**, *93*, 106808; m) L. Tao, Z. Xu, C. Kuai, X. Zheng, C. E. Wall, C. Jiang, A. R. Esker, Z. Zheng, F. Lin, *Energy Storage Mater.* **2020**, *24*, 129; n) L. Tao, A. Hu, Z. Yang, Z. Xu, C. E. Wall, A. R. Esker, Z. Zheng, F. Lin, *Adv. Funct. Mater.* **2020**, *30*, 2000585.

[5] a) X. Fan, E. Hu, X. Ji, Y. Zhu, F. Han, S. Hwang, J. Liu, S. Bak, Z. Ma, T. Gao, *Nat. Commun.* **2018**, *9*, 2324; b) A. Bhargav, J. He, A. Gupta, A. Manthiram, *Joule* **2020**, *4*, 285.

[6] C. Niu, D. Liu, J. A. Lochala, C. S. Anderson, X. Cao, M. E. Gross, W. Xu, J.-G. Zhang, M. S. Whittingham, J. Xiao, *Nat. Energy* **2021**, *6*, 723.

[7] a) F. N. Jiang, S. J. Yang, H. Liu, X. B. Cheng, L. Liu, R. Xiang, Q. Zhang, S. Kaskel, J. Q. Huang, *SusMat* **2021**, *1*, 506; b) A. J. Sanchez, E. Kazyak, Y. Chen, J. Lasso, N. P. Dasgupta, *J. Mater. Chem. A* **2021**, *9*, 21013; c) A. J. Sanchez, E. Kazyak, Y. Chen, K.-H. Chen, E. R. Pattison, N. P. Dasgupta, *ACS Energy Lett.* **2020**, *5*, 994.

[8] a) S. H. Wang, Y. X. Yin, T. T. Zuo, W. Dong, J. Y. Li, J. L. Shi, C. H. Zhang, N. W. Li, C. J. Li, Y. G. Guo, *Adv. Mater.* **2017**, *29*, 1703729; b) M. C. Stan, J. Becking, A. Kolesnikov, B. Wankmiller, J. E. Frerichs, M. R. Hansen, P. Bieker, M. Kolek, M. Winter, *Mater. Today* **2020**, *39*, 137; c) P. Qing, Z. Wu, A. Wang, S. Huang, K. Long, T. Naren, D. Chen, P. He, H. Huang, Y. Chen, *Adv. Mater.* **2023**, *35*, 2211203.

[9] a) G. Frankel, *J. Electrochem. Soc.* **1998**, *145*, 2186; b) G. Burstein, P. Pistorius, S. Mattin, *Corros. Sci.* **1993**, *35*, 57; c) L. Gireaud, S. Grugeon, S. Laruelle, B. Yrieix, J.-M. Tarascon, *Electrochem. Commun.* **2006**, *8*, 1639.

[10] J.-H. Hyun, M.-J. Yi, H. Jung, S.-H. Lee, J. H. Um, S.-H. Yu, *Energy Storage Mater.* **2023**, *54*, 146.
[11] a) X.-R. Chen, C. Yan, J.-F. Ding, H.-J. Peng, Q. Zhang, *J. Energy Chem.* **2021**, *62*, 289; b) J. Seo, W. Jeong, M. Lim, B. Choi, S. Park, Y. Jo, J.-W. Lee, H. Lee, *Energy Storage Mater.* **2023**, *60*, 102827; c) J. H. Um, S. H. Yu, *Adv. Energy Mater.* **2021**, *11*, 2003004.
[12] Y. K. Huang, R. Pan, D. Rehnlund, Z. Wang, L. Nyholm, *Adv. Energy Mater.* **2021**, *11*, 2003674.
[13] D. Wang, C. Luan, W. Zhang, X. Liu, L. Sun, Q. Liang, T. Qin, Z. Zhao, Y. Zhou, P. Wang, *Adv. Energy Mater.* **2018**, *8*, 1800650.
[14] M. Baek, J. Kim, K. Jeong, S. Yang, H. Kim, J. Lee, M. Kim, K. J. Kim, J. W. Choi, *Nat. Commun.* **2023**, *14*, 1296.
[15] F. Shi, A. Pei, D. T. Boyle, J. Xie, X. Yu, X. Zhang, Y. Cui, *Proc. Natl. Acad. Sci. USA* **2018**, *115*, 8529.
[16] Z. Wu, H. Liu, J. Holoubek, C. Anderson, L. Shi, H. Khemchandani, D. Lu, D. Liu, C. Niu, J. Xiao, *ACS Energy Lett.* **2022**, *7*, 2701.
[17] Z. Wu, C. Wang, Z. Hui, H. Liu, S. Wang, S. Yu, X. Xing, J. Holoubek, Q. Miao, H. L. Xin, *Nat. Energy* **2023**, *8*, 340.